Electric Power Systems Research 214 (2023) 108818

Contents lists available at ScienceDirect

Electric Power Systems Research

journal homepage: www.elsevier.com/locate/epsr

Optimized control strategy for single-phase multilevel cascaded converter in a distributed PV-BESS system

Pasquale Franzese [b], Mattia Ribera [b], Andrea Cervone [a], Diego Iannuzzi [b,*]

[a] École polytechnique fédérale de Lausanne (EPFL), Power Electronics Laboratory (PEL), 1015 Lausanne (VD), Switzerland
[b] Department of Electrical Engineering and Information Technology University of Naples "Federico II", Naples, Italy

ARTICLE INFO

Keywords:
Renewable Energy Sources (RES)
Modular Multilevel Cascaded Converter (MMCC)
Distributed Maximum Power Point Tracking (DMPPT)
Battery Energy Storage System (BESS)
Optimized Control Algorithm
Concentrated equivalent circuit

ABSTRACT

The paper focuses on the energy management of a single-phase PV-BESS hybrid distributed system sized for residential applications, using a CHB converter topology as grid interface. The CHB is driven with a hierarchical energy management architecture, with a single centralized controller for the upper layer, and with multiple decentralized controllers for the lower layer. The upper layer generates the reference signals to be tracked. In ideal conditions, the CHB should work with all PV modules at their MPP and with unitary power factor. This is not always possible because of some functional constraints (e.g., voltage/current constraints, partial shadowing, SoC mismatches). Therefore, a weighted sum optimization method is proposed to explicitly considers these effects and to compute a set of reference variables to be tracked, in a way to optimize the steady-state system performances while, at the same time, guaranteeing the respect of the aforementioned constraints. In this framework, different functional requirements have been included in the optimization algorithm with higher or lower priority according to different operating conditions. The optimal references are then tracked by a decentralized control layer, using standard feedback control techniques. Numerical analysis and experimental results are carried out in order to validate the optimal algorithm in typical operating conditions and to assess the effectiveness of proposed CHB configuration with the whole control strategy.

Acronyms

v_g	voltage of the grid
i_g	current of the grid
$\bar{V}_g$	phasor of the voltage of the grid
$\bar{I}_g$	phasor of the current of the grid
$u_{pv,k}$	DC voltage of the k-th PV-fed module
$i_{pv,k}$	DC current of the k-th PV-fed module
$u_{b,k}$	DC voltage of the k-th battery-fed module
$i_{b,k}$	DC current of the k-th battery-fed module
$v_{pv,k}$	AC voltage of the k-th PV-fed module
$v_{b,k}$	AC voltage of the k-th battery-fed module
$\bar{V}_{pv,k}$	phasor of the AC voltage of the k-th PV-fed module
$\bar{V}_{b,k}$	phasor of the AC voltage of the k-th battery-fed module
$u_{pv,eq}$	DC voltage of the PV-fed equivalent module
$i_{pv,eq}$	DC current of the PV-fed equivalent module
$u_{b,eq}$	DC voltage of the battery-fed equivalent module
$i_{b,eq}$	DC current of the battery-fed equivalent module
$v_{pv,eq}$	AC voltage of the PV-fed equivalent module
$v_{b,eq}$	AC voltage of the battery-fed equivalent module
$\bar{V}_{pv,eq}$	phasor of the AC voltage of the PV-fed equivalent module
$\bar{V}_{b,eq}$	phasor of the AC voltage of the battery-fed equivalent module
$p_{pv,k}$	instantaneous power of the k-th PV-fed module
$p_{b,k}$	instantaneous power of the k-th battery-fed module
$p_{pv,eq}$	instantaneous power of the PV-fed equivalent module
$p_{b,eq}$	instantaneous power of the battery-fed equivalent module
$P_{pv,k}$	active power of the k-th PV-fed module
$P_{b,k}$	active power of the k-th battery-fed module
$P_{pv,eq}$	active power of the PV-fed equivalent module
$P_{b,eq}$	active power of the battery-fed equivalent module
$SoC_{b,eq}$	weighted average of the SoC of the battery-fed modules

1. Introduction

THE ongoing growth in energy demand and the increasing environmental awareness have strengthened the need to integrate

* Corresponding author.
E-mail address: iandiego@unina.it (D. Iannuzzi).

https://doi.org/10.1016/j.epsr.2022.108818
Received 12 July 2022; Received in revised form 6 September 2022; Accepted 15 September 2022
Available online 29 September 2022

Renewable Energy Sources (RES) into the traditional power system. High penetration of RES, which are strongly volatile, has changed the grid paradigm and has led to new challenges for the grid-connected power electronic converters. The inherent modularity of RES has led to the concept of Distributed Energy Resources (DER): small-scale power plants and energy storage systems spread across the power grid and located close to the users. In particular, solar photovoltaic systems have experienced an exponential growth during the last decade, thanks to incentive programs proposed by local governments and due to the steep reduction in the cost resulting from the technology improvements.

One of the main challenges posed by the high penetration of distributed PV energy resources into the traditional power system is represented by the intermittent nature and partial shadowing phenomena of the supplied power. To tackle and overcome the above challenges, the integration of energy storage systems (ESS) with RES represents one of the more accredited solutions [1–3] .

Among different energy storage technologies, batteries have gained more attention and application due to scalable power rating, low cost, non-polluting and high reliability and efficiency. A Battery Energy Storage System (BESS) acts as an energy buffer in the PV generation system and offers several advantages. Firstly, it enhances the self-consumption of residential PV plants, by storing the energy when it is not demanded by local loads and by supplying this energy when required. Secondly, it provides some services to the utility grid, such as frequency and voltage regulation, peak shaving and load shifting. Thirdly, the integration of a distributed energy storage system allows to balance the output power provided by each sub-module and to smooth the intermittency of the power delivered to the grid. As a result, these hybrid PV-BESS systems allow a better exploitation of DER, improve the dispatching of PV resources, enhance the efficiency and the stability of the overall system and provide the operational flexibility and continuity of the power supply in case of failure.

Conventionally, a photovoltaic (PV) inverter is composed of two-stage power conversion [4,5]. At first, the low-voltage (LV) PV panel is connected to a DC/DC boost converter to obtain a DC voltage suitable for inverting. Then, a DC/AC converter is placed between the grid and the DC-link. However, multiple power conversion stages feature lower efficiency due to higher power loss, higher size-weight (associated with the switching harmonics filter and transformer) and higher costs. To overcome these limitations, high-efficiency and reliable hybrid PV-BESS systems using multilevel converters category integrated with BESS have seen a growing interest in recent years [6–10,12,13,15,18,19]. The literature survey shows that in multilevel converters category, several types have been proposed for PV power applications, such as: modular multilevel converter (MMC) [11], CHB [12,13], cascaded Z-source [14], cascaded quasi Z-source (qZS) [15], and multilevel DC-link (M-DC-link) [16,17,19,20].

Among different families of multilevel inverters, the Modular Multilevel Cascaded Converter (MMCC) has become more and more attractive for photovoltaic application, given its inherent modularity [12,13,15]. An MMCC shows a per-phase circuit configuration based on the series connection of basic converter elements, called sub-modules, typically full-bridge or half-bridge structures. This arrangement allows reaching higher voltage levels by exploiting semiconductor devices of lower voltage rating. The modularity provides several advantages: it improves the fault tolerance, since a possible faulty module can be bypassed and the whole system can still operate with reduced output voltage levels, it leads to reduced maintenance costs and facilitates the replacement of a faulty cell. Among different MMCC topologies, in this paper, the focus will be placed on the Cascaded H-Bridge (CHB) inverter. This architecture suits best for PV generation systems, since different distributed power sources can be interlinked. Furthermore, the inherent modularity of the CHB allows the implementation of a Distributed Maximum Power Point Tracking (DMPPT) by means of a proper modulation strategy. A DMPPT allows achieving a higher power harvesting, with respect to the conventional centralized architectures, when uneven operating conditions occur because of the different ageing among the cells or the partial shading phenomena.

For the CHB converters integrated with BESS, the energy storage unit is usually placed in parallel for each sub-module with the PV system to obtain controllable real and reactive power injection into the grid. For this solution, additional converters may be needed for energy storage units. Minimum hardware cost is attractive. However, different papers have focused on the CHB-based BESS in the past decades [6–14,18,23] since the battery packs are also low voltage DC sources. Many of these have proposed decentralized power management. In [23], the authors proposed a hierarchical distributed control architecture that consists of primary control for grid power tracking, secondary control based on consensus algorithm to regulate power sharing among modules and battery state of charge (SOC) balancing control to improve energy efficiency of BESS. A carrier phase shift control was also implemented to achieve multilevel output voltage and harmonic reduction. However the proposed configuration did not implement the management of PV sources. In [24], the authors proposed a full hardware implementation for a PV Module-Level CHB Inverter with BESS. Each module consists of a double stage of PV and BESS using DC-DC power converters for each stage. This allowed to overcome the operating limits of PV-CHB configurations [13,15,16]. In [25], the authors proposed both PV modules and BESS directly connected to the dc-link of each H-bridge converters. In particular, in the latter configuration the authors give a solution in terms of power management just for BESS concentrated solution (n-PV module and 1 BESS). In addition, a modified power management method was developed to adaptively modify the current power points for PV panels from their maximum power points to solve the potential overmodulation problem caused by frequent battery charging and discharging.

In this context, the paper focuses on the energy management improvement of a single-phase PV-BESS hybrid system using CHB converter topology as an interface. Part of the CHB modules is directly supplied by PV sources (n-cells), while the remaining modules are directly supplied by battery sources (m-cells). The CHB is driven with a hierarchical energy management architecture, with a single centralized controller for the upper layer (aimed at the reference signals generation), and with multiple decentralized controllers for the lower layer (aimed at the reference signals tracking). In ideal conditions, all the PV modules should work at their Maximum Power Point (MPP), and all the CHB modules should work with unitary power factor towards the grid. However, this is not always possible because of some functional constraints for the system, like voltage/current constraints, partial shadowing phenomena or SoC mismatches. Therefore, to manage the active and reactive power flow between the PV and battery modules with the main grid, the proposed energy management strategy is based on a weighted sum optimization method, that explicitly considers the aforementioned constraints and can adapt their priority according to the operating conditions of the system. The optimization algorithm is formalized to compute a set of reference variables (in the form of phasor quantities) to be tracked in steady-state conditions by the CHB converter, in order to minimize a chosen objective function while satisfying the functional constraints of the system.

The optimal references, computed by the centralized controller of the upper layer with relatively slow dynamics, are then tracked by the local controllers of the lower layers, which instead act with a faster execution rate and is implemented with standard feedback control techniques.

The main novelty of the proposed approach is related to the introduction of a weighted sum optimization method for the computation of the steady-state voltage and current references for the CHB. Additionally, this optimization has been formalized with the explicit introduction of the functional constraints of the CHB within the references computation algorithm. This makes it possible to extend the controller effectiveness in sub-optimal operating conditions without penalizing the active power generation requirements.

The paper is structured as follows. Firstly, Section 2 describes the

adopted system architecture. Secondly, Section 3 discusses analytically the proposed weighted sum optimization method. Then, Section 4 summarizes the overall architecture of the proposed hierarchical controller. Section 5 gives some numerical examples of the proposed strategy in different operating conditions, thus exploring the effects of different system constraints. Section 6 gives some simulation results to show the dynamical performances of the proposed hierarchical controller. Section 7 presents the prototype and laboratory set-up for experimental validation. Finally, Section 8 summarizes the conclusions of the paper.

2. System architecture

The topology of the proposed PV-battery hybrid system using CHB converter is shown in Fig. 1, where PV and battery modules are directly connected to the LV DC bus of full H-bridge power sub-modules. The voltage $u_{pv,k}$ and the power of PV panels vary with the solar irradiation to maximize the power supplied (MPPT), the $u_{b,k}$ change as a consequence of the SoC changing and the current flowing in the internal resistance of the cells. The power sub-module with battery works as a buffer to compensate the difference between the output power from PVs and the required power injected into the grid. As this proposed system is required to control the power flow at the converter connection and the power flow of each sub-module, a two-layer control architecture is proposed (Fig. 2):

- *Upper layer.* It consists of *central controller* which is demanded the task of computing the reference current, voltages and powers on the AC side of the CHB inverter, while respecting the constraints of the battery charge state and maximum active/reactive power and current of the individual sub-modules. At this level, main electrical quantities of each sub-modules (e.g., SoC, voltage and PV power information) are collected by means of fieldbus network and linear feedback and feedforward regulator to control the AC grid current is implemented.
- *Lower layer.* It consists of *local controllers* implemented at each sub-module which are demanded the task of MMPT algorithm of PV modules and charge/discharge control of batteries. At this level, the reference voltages of each sub-module are carried out taking into account the overall AC voltage reference calculated by central controller and the reference AC powers calculated by linear feedback and feedforward regulator of PV voltages of each sub-module. The PWM modulation is used to drive the full bridge converters to obtain a desired AC voltage.

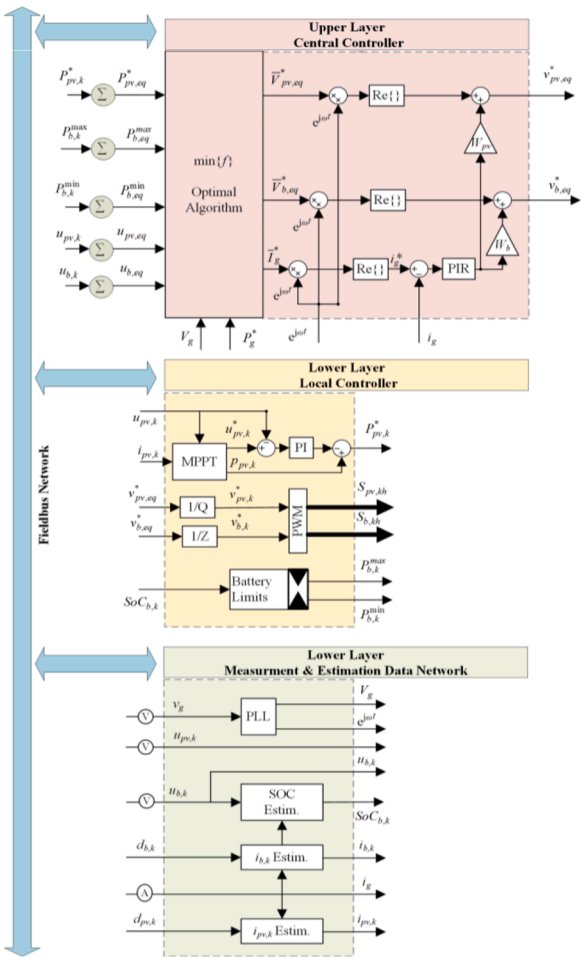

Fig. 2. Block scheme of the proposed hierarchical control algorithm. The upper layer (red) computes the voltage paths of equivalent PV panel and battery using power and voltage references and measurements. The lower layers are module specific: the yellow one provides reference values and control signals from measured or estimated values, the green one estimates the electrical not measured values.

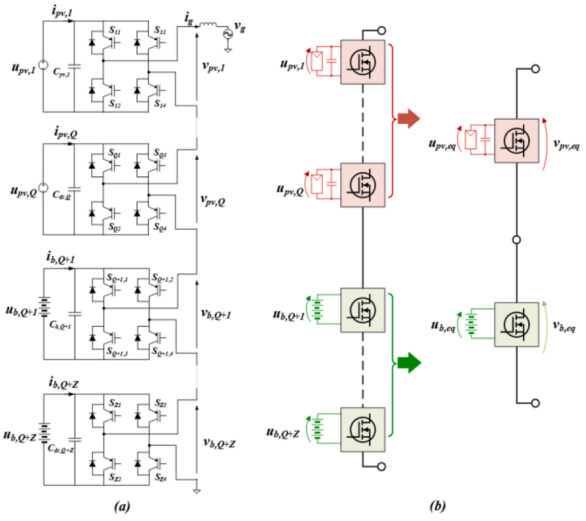

Fig. 1. CHB inverter topology: (a) CHB architecture, (b) Equivalent PV-fed and battery-fed stacks.

The MMC pulse-width-modulation can be executed though a standard reference/carrier comparison, which is however separately executed to the PV-fed and to the battery-fed stacks. Different modulation techniques may be implemented for multi-level converter [21,22,27,28]. Both Level Shifted (LS), SSPWM [27] and Phase Shifted (PS) [21,22] approaches can be used to compare the reference voltages $v^*_{pv,eq}$ and $v^*_{b,eq}$ to multiple carriers and to generate the proper switching signals to command the semiconductor devices.

The modulation can be easily modified to explicitly consider the power flow management among different MMC modules. For the PV-fed stack this can be used to compensate for unequal radiation into different PV-fed modules (i.e., panels with higher radiation are typically asked to develop more power and, therefore, their power contribution is higher). Similarly, for the battery-fed stack this power management can be conveniently used to equalize the SoC of different MMC modules. As known from the technical literature, the power management among different MMC modules can be done with sorting algorithm for LS-based modulation approaches and with some superimposed differential mode voltage injections for PS-based modulation algorithms.

3. Optimal control alghortim

As previously mentioned, in ideal conditions all the PV modules should work at their MPP, and the CHB should work with unitary power factor towards the grid. However, the presence of functional constraints may limit the system performances. Therefore, the proposed references signal computation algorithm has been based on a weighted sum optimization method, inherently considering these constraints. The topic of this section is the mathematical formulation of this optimization problem.

A *Mathematical modelling assumptions*

The basic assumptions for the mathematical model are summarized as follows:

- The system is in sinusoidal steady-state at a frequency f and angular frequency $\omega = 2\pi f$, therefore the voltages and currents can be represented by the corresponding phasors. The phasors are considered to refer to the RMS values of the sinusoidal quantities, and the AC grid voltage v_g identifies the reference axis for the phase delays, meaning that its phasor is $\bar{V}_g = V_g \cdot e^{j0} = V_g$.
- The power losses on the filtering inductor and on the converter's devices are neglected.
- The overall PV and battery modules are identified by two equivalent DC stacks, with voltage $u_{pv,eq}$ and $u_{b,eq}$ and which supply the voltages $v_{pv,eq} = \mathrm{Re}\{\bar{V}_{pv,eq} \cdot e^{j\omega t}\}$ and $v_{b,eq} = \mathrm{Re}\{\bar{V}_{b,eq} \cdot e^{j\omega t}\}$, respectively.

This control level is aimed at computing the phasors of the AC equivalent voltages of CHB photovoltaic module ($\bar{V}_{pv,eq}$), of CHB battery module, ($\bar{V}_{b,eq}$), and of the AC grid current ($\bar{I}_g$). Since each phasor is represented by two real quantities, there are *6* degrees of freedom, which are to be chosen in order to track the reference deliverable power by the panel $P^*_{pv,eq}$ and the power demanded by the grid P^*_g.

The system, however, is subject to some constraints, which make its solving more complex. The main constraints of the problem are related to the electrical constraints about circuit topology and to the voltage, current and power limits.

B *Circuit Constraints*

The system must respect the electrical equilibrium equation due to the Kirchhoff principle:

$$\bar{V}_{pv,eq},\ +\bar{V}_{b,eq} = j\omega L \cdot \bar{I}_g + \bar{V}_g \tag{1}$$

that is a complex equation and represents two scalar equality constraints.

C *Voltage Constraints*

The AC voltage $v_{pv,eq} = \mathrm{Re}\{\bar{V}_{pv,eq} \cdot e^{j\omega t}\}$of the equivalent PV-fed module is limited by the DC voltage $u_{pv,eq}$ of the equivalent panel itself:

$$\left|\bar{V}_{pv,eq}\right| \le u_{pv,eq} \Big/ \sqrt{2} \Rightarrow \bar{V}_{pv,eq} \cdot \hat{\bar{V}}_{pv,eq} \le u^2_{pv,eq} \Big/ 2 \tag{2}$$

The AC voltage $v_{b,eq} = \mathrm{Re}\{\bar{V}_{b,eq} \cdot e^{j\omega t}\}$ of the equivalent battery-fed module is limited by the DC voltage $u_{b,\mathrm{eq}}$ of the equivalent battery itself:

$$\left|\bar{V}_{b,eq}\right| \le u_{b,\mathrm{eq}} \Big/ \sqrt{2} \Rightarrow \bar{V}_{b,eq} \cdot \hat{\bar{V}}_{b,eq} \le u^2_{b,\mathrm{eq}} \Big/ 2 \tag{3}$$

D *Current Constraint*

The AC current $i_g = \mathrm{Re}\{\bar{I}_g \cdot e^{j\omega t}\}$ is limited to a maximum value $I_{g,max}$ allowed by the conversion devices, the equivalent battery stack and the equivalent panel stack:

$$\left|\bar{\boldsymbol{I}}_{\boldsymbol{g}}\right| \le I_{g,\max} \Big/ \sqrt{2} \Rightarrow \bar{\boldsymbol{I}}_{\boldsymbol{g}} \cdot \hat{\bar{\boldsymbol{I}}}_{\boldsymbol{g}} \le I^2_{g,\max} \Big/ 2 \tag{4}$$

E *Power Constraints*

The power flow of the converter on the PV panel module must be unidirectional, from the DC side to the AC side:

$$P_{pv,eq} = \mathrm{Re}\left\{\bar{V}_{pv,eq} \cdot \hat{\bar{I}}_g\right\} \ge 0 \tag{5}$$

The MPPT algorithm on the converter on the photovoltaic module works in a certain voltage range, so if the voltage of the panel falls below a certain threshold, the supply decreases until it stops. This constraint can be formalized by introducing a function $P^{\max}_{pv,eq}(u_{pv,eq})$:

$$P_{pv,eq} = \mathrm{Re}\left\{\bar{V}_{pv,eq} \cdot \hat{\bar{I}}_g\right\} \le P^{\max}_{pv,eq}\left(u_{pv,eq}\right) \tag{6}$$

such that, at the minimum threshold, it results $P^{\max}_{pv,eq}(u^{\min}_{pv,eq}) = 0$.

The equivalent battery stack limit power flow is based on its SoC. In other words, the battery supplies a positive or negative power in order to balance the power exchange between modules and the network; if the battery is almost completely discharged its delivered power cannot be positive, while if the battery is fully charged its delivered power cannot be negative.

$$\boldsymbol{SoC_{b,\mathrm{eq}}} < 20\%\ \mathrm{v}\ \boldsymbol{SoC_{b,\mathrm{eq}}} \cong 100\% \Rightarrow \boldsymbol{P_{b,eq}} = 0 \tag{7}$$

By introducing two functions $P^{max}_{\mathrm{b,eq}}(SoC_{\mathrm{b,eq}}) \ge 0$ and $P^{min}_{\mathrm{b,eq}}(SoC_{\mathrm{b,eq}}) \le 0$, this can be modelled as:

$$P_{b,eq} = \mathrm{Re}\left\{\bar{V}_{b,eq} \cdot \hat{\bar{I}}_g\right\} \le P^{\max}_{b,eq}\left(SoC_{b,eq}\right) \tag{8}$$

$$P_{b,eq} = \mathrm{Re}\left\{\bar{V}_{b,eq} \cdot \hat{\bar{I}}_g\right\} \ge P^{\min}_{b,eq}\left(SoC_{b,eq}\right) \tag{9}$$

where the minimum and maximum SoC have been selected as 20% and 80% of the rated battery capacity.

F *Functional Requirements*

The constraints from (1) to (9) already analyzed define the operative range of the system and must always be satisfied. For the proposed modelling, the functional requirements of the system can also be treated as additional constraints, yet with a lower priority (i.e. they should be satisfied only if they are not in contrast with all the other constraints).

With this approach, the power supplied to the grid must have the constant value:

$$P^*_g = \mathrm{Re}\left\{\bar{V}_g \cdot \hat{\bar{I}}_g\right\} \tag{10}$$

The power delivered by the photovoltaic module must be as close to that chosen by the MPPT algorithm as:

$$P^*_{pv,eq} = \mathrm{Re}\left\{\bar{V}_{pv,eq} \cdot \hat{\bar{I}}_g\right\} \tag{11}$$

The power constraints P^*_g and $P^*_{pv,eq}$cannot always be satisfied. Some simple examples are following cases:

- If the power supplied by the photovoltaic module is lower than the power required by the grid and the battery is completely discharged, the power supplied to the grid will be lower, but the system must continue to operate.
- If the power required by the network is lower than that chosen by the MPPT algorithm and the battery is fully *charged*, the panel will be made to work at the power required by the network (without the MPPT algorithm).

- If the overall equivalent DC voltages are not capable of satisfying the grid and the PV power requirements at the same time, or if the required grid current exceeds its feasible limits, the algorithm must find a trade-off condition.

G *Multi-Objective Optimization Formulation*

To mathematically solve this weighted sum optimization problem with different priority levels, it is possible to formulate a single weighted sum optimization function. Based on the weighted sum method, a linear combination of all constraints, multiplied by specific weights, is minimized to solve the optimal problem.

Therefore, the constraints (10) and (11) can be relaxed and considered as an integral part of the objective function.

The chosen multi-objective function of the optimization problem is shown below:

$$\min \sum_{i=1}^{4} f_i : \begin{cases} f_1 = c_1 \ \mathrm{Im}\{\bar{V}_g \cdot \hat{\bar{I}}_g\}^2 \\ f_2 = c_2 \left(\mathrm{Im}\{\bar{V}_{pv,eq} \cdot \hat{\bar{I}}_g\}^2 + \mathrm{Im}\{\bar{V}_{b,eq} \cdot \hat{\bar{I}}_g\}^2 \right) \\ f_3 = c_3 \left(P_g^* - \mathrm{Re}\{\bar{V}_g \cdot \hat{\bar{I}}_g\} \right)^2 \\ f_4 = c_4 \left(P_{pv,eq}^* - \mathrm{Re}\{\bar{V}_{pv,eq} \cdot \hat{\bar{I}}_g\} \right)^2 \end{cases} \quad (12)$$

The terms of (12) are respectively utilized to minimize:

- the total reactive power of the grid;
- the sum of the reactive power of PV and battery modules;
- the displacement between desired power and actual power provided to the grid;
- the displacement between desired power, and the actual power absorbed by the photovoltaic panel module.

The gains $\{c_1, c_2, c_3, c_4\}$ in (12) are non-dimensional terms defining the priority of each term in the weighted sum optimization method. Higher values of such gains are associated to higher priority tasks, and lower values with lower-priority tasks. Therefore, they can be chosen in a different way according to operating condition.

For the examined application, the reactive power minimization is considered as being a low-priority task, thus related to "low" values for $\{c_1, c_2\}$, while the active power tracking is considered as being a high-priority task, thus related to "high" values for $\{c_3, c_4\}$. Additionally, the gains $\{c_3, c_4\}$ are also updated in real time according to the reference active powers P_g^* and $P_{pv,eq}^*$ and to the overall state of charge of the battery pack. They follow the scheme represented in Table I, which can be interpreted as follows:

- for reduced values of the SoC, the battery cannot supply the required power when $P_g^* > P_{pv,eq}^*$; since $P_{pv,eq}^*$ cannot be increased, the grid power seeking is given a lower priority (i.e. $c_4 \gg c_3$),
- for high values of the SoC, the battery cannot store the surplus power when $P_{pv,eq}^* > P_g^*$; since P_g^* cannot be increased, the PV power seeking is given a lower priority (i.e. $c_3 \gg c_4$),
- for intermediate values of the SoC, the battery can behave effectively and both the grid and the PV power seeking requirements can be given a similar priority.

The minimization of (12) can be achieved with any standard iterative algorithm employed to solve optimization problems (e.g., gradient-descent based methods). For real-time applications, since the operation refers to steady-state conditions, the optimization can be executed with reduced execution rate (e.g., several *ms*), meaning that it does not represent an excessive computational burden for modern controllers. Generally speaking, higher values of the gains $\{c_1, c_2, c_3, c_4\}$ are associated with a more robust seeking of the global optimum but may require more iterations to converge. Differences of 1-2 order of magnitudes in the gains are typically enough to differentiate the task priorities with a sufficient degree of accuracy.

It is worth emphasizing that, when the system operates far from the previously discussed inequality constraints, all the terms in (12) are close to zero, and the CHB can work with unitary power factor and with the PV modules at their MPP.

4. Control scheme

The block scheme of the proposed control algorithm is schematically represented in Fig. 2 and is here discussed. First, the PV distributed local controller (lower level of Fig. 2) is executed. The MPPT algorithm, based on the measured PV voltage $u_{pv,k}$ and on the estimated PV current $i_{pv,k}$, computes a reference operating voltage $u_{pv,k}^*$ to maximize the power supplied by the k-th module. In the considered case, a standard Perturbe And Observe (P&O) MPPT algorithm has been locally implemented on each PV-powered module. However, other MPPT algorithms could have been applied without affecting the proposed control technique, that indeed only requires the knowledge of $P_{pv,k}^*$ and $u_{pv,k}$. At the same time, the same block also computes the actual PV power $p_{pv,k} = u_{pv,k} \cdot i_{pv,k}$. A simple Proportional-Integral (PI) controller, by comparing $u_{pv,k}^*$ to $u_{pv,k}$, adjusts the reference AC active power $P_{pv,k}^*$ of the PV conversion module. In steady state conditions it results $u_{pv,k}^* = u_{pv,k}$ and, by neglecting the conversion losses, $P_{pv,k}^* = P_{pv,k}$. After that, the battery management control (the green subsystem of Fig. 2) is executed. From the measured battery voltage $u_{b,k}$ and the estimated battery current $i_{b,k}$, the battery state of charge $SOC_{b,k}$ is estimated, which allows to determine the power limits of the battery stack. By neglecting the conversion losses, the maximum AC power of the conversion module $P_{b,k}^{max}$ is the battery limit power in discharging, while the minimum AC power of the conversion module $P_{b,k}^{min}$ is the battery limit power in charging. Then, each voltage, current and active power of each sub-module (PV and battery) are summed in order to obtain the equivalent DC and AC quantities.

Given the AC grid required power P_g^* and having computed all the other relevant data, the proposed optimization algorithm is executed in a way to compute the steady state phasors of the reference AC voltage generated by the PV-supplied module $\bar{V}_{pv,eq}$, of the reference AC voltage generated by the battery-supplied module $\bar{V}_{b,eq}$, and of the reference AC current $\bar{I}_g$.

The conversion modules control (the red subsystem of the Fig. 2) is then executed. A Phase-Locked Loop (PLL) is used to obtain the magnitude V_g and the instantaneous phase angle ωt of the measured grid voltage v_g. The unitary norm rotating vector $e^{j\omega t}$ is generated and is used to compute the instantaneous reference current $i_g^* = \mathrm{Re}\{\bar{I}_g \cdot e^{j\omega t}\}$. This current reference is compared to the measured current i_g and the error is processed with a Proportional-Integral-Resonant (PIR) controller tuned at the angular frequency ω. The reference voltages for the PV-supplied module $v_{pv,k}^*$ and for the battery-supplied module $v_{b,k}^*$ are both obtained as the sum of two terms: the feedforward voltage terms $v_{pv,k}^{*\,'} = \mathrm{Re}\{\bar{V}_{pv,k}^{'} \cdot e^{j\omega t}\}$ and $v_{b,k}^{*\,'} = \mathrm{Re}\{\bar{V}_{b,k}^{'} \cdot e^{j\omega t}\}$(which are computed from the steady state optimal phasors), and the feedback voltage terms $v_{pv,k}^{*\,''}$ and $v_{b,k}^{*\,''}$(which are proportional to the grid current controller output via the weights W_p and W_b).

The Pulse-Width-Modulation algorithms (the yellow subsystem in Fig. 2) are implemented to compute the conversion modules' switching signals from the reference voltages $v_{pv,k}^*$ and $v_{b,k}^*$, respectively. For the considered control, a standard unipolar modulation is applied individually for each module of the CHB. The carriers of different modules are

all triangular signals varying between 0 and 1 with the same carrier frequency f_c. The carriers are shifted with one another by $T_c/2N$, with $T_c = 1/f_c$ denoting the carrier period and N denoting the overall number of CHB modules, including both the PV-powered and the BESS-powered ones. For Unbalanced DC voltage sources, a Generalized Phase-Shifted Angles by Using Phasor Diagrams [26] was implemented.

From the knowledge of the duty-cycles $d_{pv,k}$ and $d_{b,k}$ it is possible to estimate the DC-currents $i_{pv,k}$ and $i_{b,k}$ (the green subsystem of Fig. 2).

The different blocks of the proposed algorithm can be executed at different time scales to facilitate the real-time implementation and decouple the dynamic behavior of different physical phenomena. To be more specific, by referring to the grid frequency f, the PWM, current control and DC current estimation blocks (which only require simple calculations) can be executed with a high frequency (e.g. $50 \div 100\, f$), the references computation block (which requires an iterative optimization routine) can be executed with the same time scale of f (e.g. $0.2 \div 1\, f$), and the MPPT and battery management blocks (which involve slow dynamics) can be executed with a low frequency (e.g. $0.01 \div 0.02\, f$).

5. Numerical analysis

The developed strategy has been numerically validated for a system sized for residential units' applications. The optimization problem is then solved in Matlab using the interior-point method in '*fmincon*'. The electrical setup consists of two PV and two battery sub-modules: the PV sub-modules are strings with 5 PV panels in series (2 × 1P5S), the battery sub-modules are strings with 50 cells in series (2 × 1P50S). The main parameters of the structure are summarized in Table 2.

For the considered application, the coefficients C_1 and C_2 have been set to 1 and 0.5 respectively. The coefficients C_3 and C_4 have been instead dynamically updated between the values 10 and 100 according to the guideline given in Table 1 of Section 3. This section analyses the steady-state results of the proposed optimization strategy in different operating conditions. The results are discussed by observing the phasor diagrams of the complex variables computed by solving the weighted sum optimization problem discussed in Section 3.

A *Operation within the inequality constraints boundaries*

First, consider the case in which $P_g^* \geq P_{pv,eq}^*$ and SoC of the battery stack is within the minimum and maximum of available range. This case is exemplified by the phasor diagrams of Fig. 3. In Fig. 3a ($P_g^* = P_{pv,eq}^*$), the battery stack doesn't have to provide power to the system: the reference phasor $\bar{V}_{pv,eq}$ for the equivalent PV-fed CHB stack is almost equal to the grid voltage phasor $\bar{V}_g = V_g$, the grid current phasor $\bar{I}_g$ is in phase with the grid voltage, and the reference phasor $\bar{V}_{b,eq}$ for the equivalent battery-fed stack has to compensate for the inductive voltage drop on the filtering inductance. In Fig. 3b ($P_g^* > P_{p,eq}^*$), the battery stack has to compensate for the residual power $P_{b,eq}^* \cong P_g^* - P_{pv,eq}^*$ required by the grid. In this case, the phasor of the grid current $\bar{I}_g$ is the same as in the previous case, but the overall output voltage of the CHB is shared by the PV-fed modules and the battery-fed modules according to their reference power. As an example, in this case where $P_{pv,eq}^* \cong 2P_{b,eq}^*$ (i.e. 2 kW and 1 kW), the phasors $\bar{V}_{pv,eq}$ and $\bar{V}_{b,eq}$ are almost in phase and it results $|\bar{V}_{pv,eq}| \cong 2|\bar{V}_{b,eq}|$. Higher power reference differences, $P_{b,eq}^*$, would lead to similar results, progressively decreasing the magnitude of $\bar{V}_{pv,eq}$ and increasing the magnitude of $\bar{V}_{b,eq}$.

Table 1
– Dynamic Updating of the Optimization Gains

	$P_g^* \geq P_{pv,eq}^*$	$P_g^* < P_{pv,eq}^*$
$SoC < SoC_{min}$	$c_3 \ll c_4$	$c_3 < c_4$
$SoC_{min} \leq SoC \leq SoC_{max}$	$c_3 \cong c_4$	$c_3 \cong c_4$
$SoC > SoC_{max}$	$c_3 \gg c_4$	$c_3 > c_4$

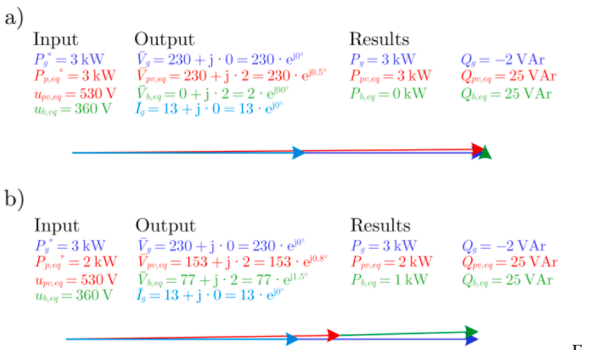

Fig. 3. Phasor diagram in the operating case in which the SoC of the battery stack has an intermediate value and (a) $P_g^* = P_{p,eq}^*$ or (b) $P_g^* > P_{p,eq}^*$.

B *Operation with SoC in edge values*

Let consider now the case where $P_g^* > P_{pv,eq}^*$, and $SoC \leq 20\%$. In this condition, the battery stack cannot provide the residual power $P_g^* - P_{p,eq}^*$ to the grid, and the PV stack (which is already working in its MPP) cannot supply any more power. Therefore, it is impossible to satisfy the power requirement of the grid, and the proposed algorithm can only lead to $P_g \cong P_{pv,eq} \cong P_{pv,eq}^*$, by reducing the gain of c_3 in according to Table 1. This case is exemplified in the phasor diagram of Fig. 4a, where it can be noted that the grid output power, whose reference is 3 kW, is limited to 2 kW, and the overall system works similarly to the case study of Fig. 3a (with only a lower magnitude for $\bar{I}_g$).

A similar problem arises when $P_g^* < P_{pv,eq}^*$, but the $SoC \geq 80\%$. Indeed, in this case, the battery stack cannot store the surplus power $P_{pv,eq}^* - P_g^*$ and, consequently, the proposed algorithm reduces the gain c_4 and gives priority to the power grid seeking requirement. The overall PV-fed power is then decreased until $P_{pv,eq} \cong P_g \cong P_g^*$, meaning that the PV panels cannot work in their MPP. An example is shown in the phasor diagram of Fig. 4b, where it can be seen that the PV power, whose reference is 3 kW, is reduced to the grid reference power of 2 kW. In this case, the voltages and current phasors are the same as in Fig. 4a.

C *Operation in case of voltage limitations*

Finally, it is worth analyzing the behavior of the proposed algorithm in case $P_g^* < P_{pv,eq}^*$, but when the SoC of the battery stack allows storing the surplus power $P_{pv,eq}^* - P_g^*$. In this case, it would be desirable to keep

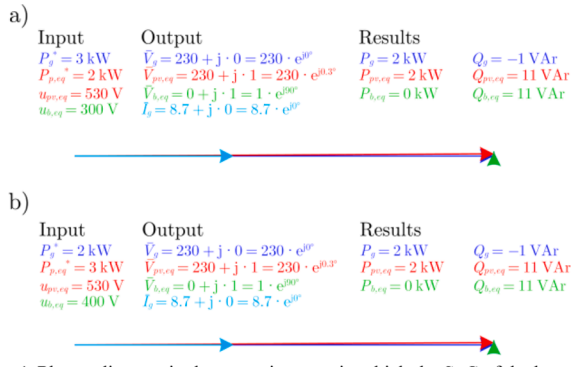

Fig. 4. Phasor diagram in the operating case in which the SoC of the battery stack has an edge value and (a) $P_g^* > P_{p,eq}^*$ or (b) $P_g^* < P_{p,eq}^*$.

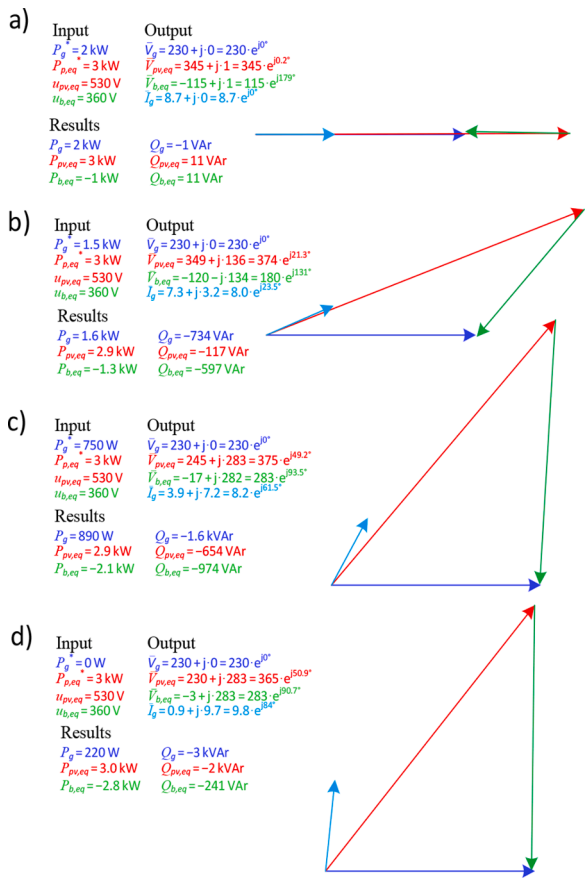

Fig. 5. Phasor diagram in the operating case in which the $P^*_{p,eq}$is constant and the P^*_g decreases.

the PV panels work at their MPP, while not altering the power transferred to the grid. The results are depicted in Fig. 5 for different values of the grid reference power P^*_g. First, when the $P^*_{pv,eq}$ is close to P^*_g, the phasor diagram is represented in Fig. 5a. The phasor grid current $\bar{I}_g$ is again in phase with the grid voltage $\bar{V}_g$, and its magnitude is related to the reference grid power P^*_g. The phasors of the equivalent PV-fed stack $\bar{V}_{pv,eq}$ and battery-fed stack $\bar{V}_{b,eq}$ are instead in phase opposition with one another, in a way that the resulting output power of the PV-fed stack is positive (the PV panels supply power), and the resulting output power of the battery-fed stack is negative (batteries are charging).

This scenario minimizes the overall reactive power of the system, but it may require the magnitude of $\bar{V}_{pv,eq}$ to be significantly higher than the magnitude of $\bar{V}_g$, as shown in Fig. 5a. In this case, the maximum magnitude of $\bar{V}_{pv,eq}$ is reached, the phase angles of the phasors can be modified in order to simultaneously satisfy both the grid and the PV power seeking requirements. This is shown in the phasor diagrams of Fig. 5b and Fig. 5c. The voltage phasor $\bar{V}_{pv,eq}$ is anticipated with respect to $\bar{V}_g$, and the voltage phasor $\bar{V}_{b,eq}$ is not anymore in phase opposition to it. The current phasor $\bar{I}_g$ is also anticipated, in a way that both the grid and the PV powers are fulfilled. Even though, the tracking of active power is satisfied, the achievement of voltage saturation limits introduces a non-zero reactive power to the grid. The extreme case is shown in Fig. 5d, where the reference grid power is zero, while the reference PV power is again equal to $P^*_{pv,eq} = 3$ kW. In this case, to make the grid active power to be almost zero, the phasor $\bar{I}_g$ is almost in quadrature with the grid voltage phasor $\bar{V}_g$. However, the voltage phasors of the equivalent PV-fed stack and of the battery-stack, thanks to their high phase angles, can still provide a positive and a negative power, respectively. As a result, the proposed approach reveals able to transfer all the PV power to the batteries, making it possible to still work around the MPP of the RES.

6. simulation results

The proposed strategy has been validated for a real-time application with numerical simulations in the MATLAB/Simulink environment. As also summarized in Table 2, the high-frequency control actions (including the PLL, the feedback current control, the PWM modulation and the estimation of the DC current) have been executed with a frequency of 10 kHz. The proposed optimization algorithm has been executed at the frequency of 25 Hz (i.e. once every two fundamental periods of the grid). The low-frequency tasks (including the MPPT of the PV-fed modules, and the SoC estimation of the battery-fed modules) have been executed with a frequency of 0.5 Hz (i.e. once every 2 s). The different transitions rates have been tackled with simple Sample and Hold functions. A standard phase-shifted modulation technique has been implemented to control the switching behavior of the converter. A standard voltage reference redistribution has been used to achieve the internal power management among the different CHB modules. For the PV-fed modules, the reference voltages have been set proportionally to their MPPT powers, in a way to compensate for partial shadowing phenomena. For the battery-fed modules, instead, the reference voltages have been set proportionally to the SoC of each single battery, in a way to compensate for potential unbalances effects.

The testing scenario has been chosen to highlight the dynamic behavior of the proposed algorithm. The system starts from steady-state conditions. The two panels are working in their MPP, but they are not equally irradiated and their MPP power are equal to 1.4 kW and 1.6 kW, respectively. The reference power required from the grid is equal to $P^*_g = 3$ kW, and perfectly compensate the overall reference power of the PV-fed stack, which is also equal to $P^*_{pv,eq} = 3$ kW. The two battery modules (whose SoC are at 49% and 51%, respectively) are not required both to provide power to the grid and to store power from the PV sources. At beginning, the reference power of the grid P^*_g is changed, and linearly decreases from 3 kW to 0 kW in a 60 s time interval. The reference power of the PV system is instead kept unchanged, meaning that the PV panels are still required to work according to their MPPT algorithms, and that their energy needs to be progressively transferred to the battery-fed modules.

Table 2
– System Parameters

	Value	Unit
Grid		
Total number of modules	4	-
Rated Power	3.3	kVA
Rated AC voltage (RMS)	230	V
Rated AC current (RMS)	15	A
Rated frequency	50	Hz
Filtering Inductance	1	mH
PV-fed modules (2 × 1P5S)		
Number of PV-fed modules	2	-
MPP power (single module)	1.48	kW
MPP voltage (single module)	263.5	V
MPP current (single module)	5.6	A
Open Circuit voltage (single module)	318.5	V
Short Circuit current (single module)	6	A
Battery-fed modules (2 × 1P50S)		
Number of battery-fed modules	2	-
Rated capacity (single module)	5	Ah
Rated voltage (single module)	180	V
Maximum voltage (single module)	210	V
Minimum voltage (single module)	150	V
Switching and lower control frequency	10	kHz
Upper control frequency	25	Hz
MPPT frequency	0.5	Hz

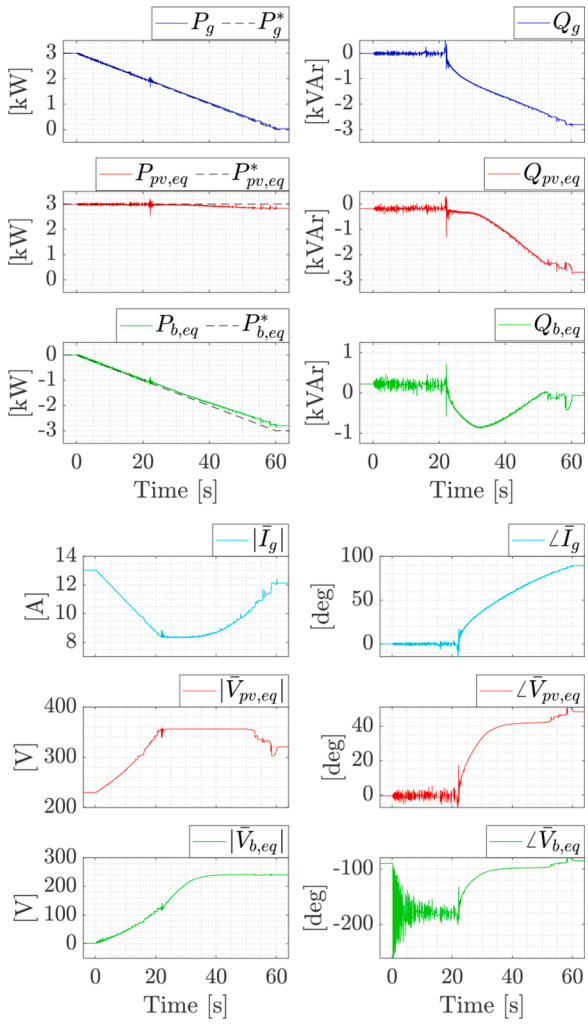

Fig. 6. Simulation of the optimization strategy with $P_{p,eq}^* = 3$ kW and P_g^* linearly decreasing.

The results are depicted in Fig. 6: the plot of the active and reactive powers of the grid $\{P_g, Q_g\}$, of the equivalent PV-fed stack $\{P_{pv,eq}, Q_{pv,eq}\}$, of the equivalent battery-fed stack $\{P_{b,eq}, Q_{b,eq}\}$ and the corresponding phasors of $\bar{I}_g$, $\bar{V}_{pv,eq}$ and $\bar{V}_{b,eq}$ in magnitude and phase are shown. The active powers are compared with the corresponding references given as input of the optimization algorithm (dashed lines, with $P_{b,eq}^* = P_g^* - P_{pv,eq}^*$). Coherently with the phasor diagrams of the previous section, the grid-related quantities are traced in blue, the PV-related quantities in red and the battery-related quantities in green. The current $\bar{I}_g$ has been traced in cyan. It can be noted that an accurate seeking of the reference active power of the grid P_g^* is achieved, while at the same time guaranteeing a close supply of the reference power from the PV panels, which can still work very close to their MPP. Initially (for the first 25 s), the decrease of the power P_g^* is achieved through a progressive increase of the magnitudes of $\bar{V}_{pv,eq}$ and $\bar{V}_{b,eq}$ (which, coherently with Fig. 5a, are in phase opposition) and a decrease of the magnitude of $\bar{I}_g$. All the reactive powers are close to zero. The saturation occurs when $\bar{V}_{pv,eq}$ reaches its maximum value (related to the measured equivalent DC voltage $u_{pv,eq}$), and the algorithm starts changing the phase angles of the phasors as described in Section 5. This changes the reactive power of the system but allows to keep tracking the reference active powers. In the time range 0-20s, the voltage phase of battery voltage change drastically. Since the charging power $|P_{b,eq}|$ is increasing, the magnitude $|\bar{V}_{b,eq}|$ of the AC voltage generated by the battery-powered modules increases, too. During the initial interval, the voltage generated by the PV-powered module has a high magnitude $|\bar{V}_{pv,eq}|$ (i.e., higher than the grid voltage itself), and is almost entirely aligned along the real axis (i.e., the phase $\angle\bar{V}_{pv,eq}$ is close to zero). Following the grid active power change, the real axis component of $\bar{V}_{pv,eq}$ increases (because of the decrease of the current $\bar{I}_g$). Because of the optimization routine, that acts iteratively on a time-changing reference, there appears a small quadrature axis component in $\bar{V}_{pv,eq}$, that oscillates around zero. This results in the small phase oscillations in the $\angle\bar{V}_{pv,eq}$ graph. To correctly balance the quadrature axis component of $\bar{V}_{pv,eq}$, also $\bar{V}_{b,eq}$ needs to produce a quadrature axis component, that oscillates around zero, too. However, since (initially) the real axis component of $\bar{V}_{b,eq}$ is small, even small quadrature axis components in $\bar{V}_{b,eq}$ result in relatively high oscillations in the computed phase angle $\angle\bar{V}_{b,eq}$, that initially varies from around -90° (i.e., a negative quadrature axis component) to around -270° (i.e., +90°, which is a positive quadrature axis component). With the increase of the real-axis component of $\bar{V}_{b,eq}$ (which, actually, increase in the negative real-axis direction, to compensate for the increase of the real axis component of $\bar{V}_{pv,eq}$), the small oscillations of the quadrature axis component around zero become less and less relevant in the computation of the phase angle, that gradually stabilizes around -180° (i.e., $\bar{V}_{b,eq}$ almost entirely lies on the real axis, and it is almost in phase opposition to $\bar{V}_{pv,eq}$ and $\bar{I}_g$, indicating a charging of the batteries).

The Fig. 7 shows the steady state results in the same operating conditions of Fig. 3b. It shows the overall output voltage realized by the CHB, the grid current and the grid voltage. It can be seen, that, coherently with the previous analysis, the current is in phase with the grid voltage. The unequal steps of the modulation are related to the different voltage values of the CHB modules. In this operating condition the total harmonic distortion, THD, is equal to 4.64% lower than 5%. Thus, the current distortion limit for general distribution system is complied with the IEEE 519 standard in term of power quality. In the other operating conditions shown in Figs. 3a, 4a and 4b, the THD is equal to 2.54%, 4.83%, and 4.26% respectively.

Fig. 8 shows the steady state results in the same operating conditions of Fig. 5b. It can be seen that, in this case, the current is not anymore in phase with the grid voltage. The PWM voltage is different from the previous case because the voltages $v_{pv,eq}$ and $v_{b,eq}$ are not in phase with one another. A worsening of power quality in term of grid current distortion is observed, the THD is equal to 4.94%. This suggests an improving of PWM modulation technique or the need to also include a power quality constraint in the optimal control strategy [29,30].

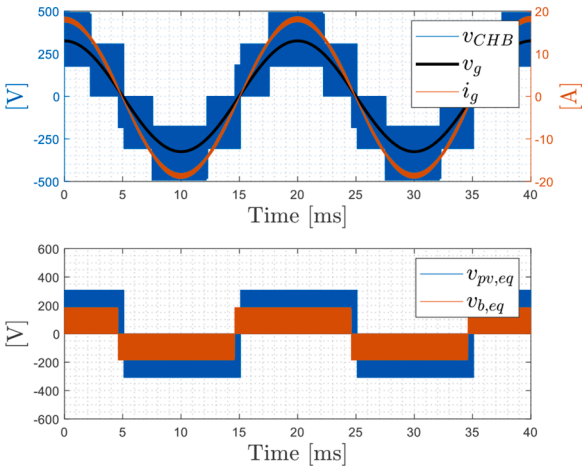

Fig. 7. Results of modulation in the same condition of Fig. 3b. (a) Voltage and current on the grid and the AC modulated voltage of the entire series of converters, (b) the AC modulated voltage on the equivalent PV and BESS modules.

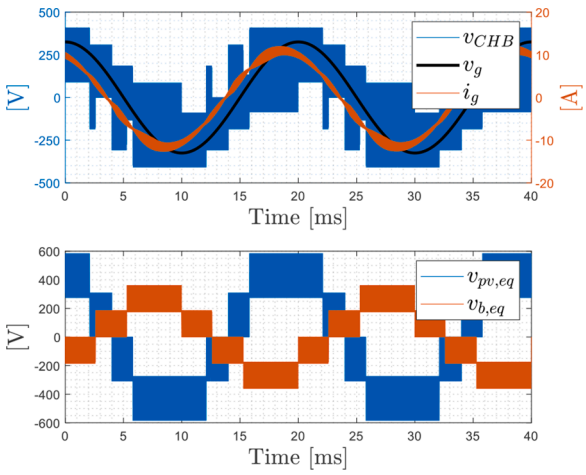

Fig. 8. Results of modulation in the same condition of Fig. 5b. (a) Voltage and current on the grid and the AC modulated voltage of the entire series of converters, (b) the AC modulated voltage on the equivalent PV and BESS modules.

Nevertheless, an increasing of number of CHB modules and a designed L filter can significantly improve the power quality of the CHB in this operating condition. In the other operating conditions shown in Fig. 5a, 5c and 5d, the THD is equal to 4.90%, 4.02%, and 3.46% respectively. Other aspects like the weak grid conditions or the faulty scenarios have not been considered since the considered architecture is targeted to low-voltage residential applications, where the relatively low power levels, compared to the grid, generally make the assumption of a strong grid to be acceptable. However, for the case of grid-following converter connected to a weak grid, we would like to address that a simple approach that could immediately allow an extension of the proposed technique would just require considering the equivalent grid impedance together with the filtering inductance in (1). Under this perspective, the grid impedance at the fundamental frequency ω can be simply modeled through the lumped parameters of a series R-L filter, that can be easily added to the electrical Eq. (1). The only other difference would be needed for the PLL algorithm, which would require estimating the grid instantaneous angle without being severely affected by the operating conditions (i.e., by the magnitude and phase angle of the controlled current). However, the rest of the optimization algorithm (which is the core of the work) and the inner control loops do not need any modification with respect to the ones presented in the paper. Despite the presence of an additional impedance in the grid, the proposed control strategy can still manage to properly track the reference active powers, while keeping the reactive powers at reduced values.

7. Experimental validation

A *Experimental Set-up and Control Implemetation*

In order to experimentally validate the proposed configuration and control approach, a downsized prototype of a grid-tied PV modular CHB inverter was built, as shown in Fig. 9 (a). To have replicable conditions in the experimental tests the PV sources were simulated with two AMETEK Programmable Photovoltaic Simulator ELGAR ETS80 × 10.5C-PVF with a maximum rated power of 800 W (i.e. 80 V, 10 A). They were remotely controlled with the dedicated Terra SAS Software, which offers the possibility of defining the desired V-I PV curve and visualizing the operating point in real-time on a dedicated computer. Each PV simulator was programmed to supply the two profile of an individual PV module, with $P_{MPPT} = 150$ W corresponding to $V_{MPPT} = 29.5$ V and $I_{MPPT} = 5$ A at STC. The fill factor was set up 0.746. According to the two curves in the irradiation range of [200 W/m^2, 1000 W/m^2], the lower boundary, $v_{pv_{min}}$, of the MPPT range was set to 2.5 V. The BESS sources were simulated with the Elektro-Automatik Power Supply EA-PS 8360-15 (BESS1) and the Programmable Switching Power Supply ITECH IT6500C (BESS2). Four equal H-bridge cells were realized with Infineon components IRGB4056DPbF which are IGBT with anti-parallel diode, they were welded on a PCB together with drivers. A single cell was shown in Fig. 9 (b). Capacitances were added in parallel to all the sources to stabilize the working point, the capacitance value should not be lower than 2.9mF. Electrolytic capacitors AYX-HR of 3300μF were used. All the H-bridge modules were equipped with LEM LV-25-P to measure the DC-Link voltage. The AC current was measured with a LEM LA-35-NP, while the grid voltage was measured with LEM DVL 500 and visualized on Keysight Infinii Vision DSO-X 2014A Scope. Table 3- illustrates the reference values for the system when the proposed down-scaling was adopted. The inductance of line filter inductor was $L = 5$ mH., the inverter output was connected to the single-phase grid through a Variac (variable alternating current transformer) in order to obtain a suitable downsized grid level. The transformer secondary side

Table 3
DOWN-SCALED SYSTEM SIZING

Description	Symbol	Value	Unit
Rated Grid Power	P_{grid}	138	W
MPPT Power single module	$P_{PV,j}$	150	W
Grid voltage	$V_{grid,RMS}$	46	V
DC-Link Voltage per PV module	V_{MPPT}	30	V
DC-Link Voltage per BESS module	V_{BESS}	36	V
MPPT current	I_{MPPT}	5	A
Nominal AC current RMS	I_{max}	3	A

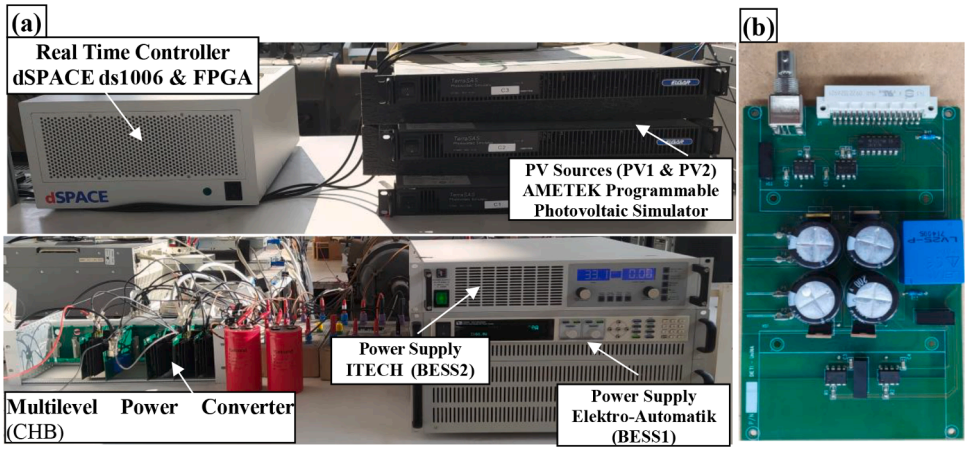

Fig. 9. - Lab hardware prototype: (a) Hardware implementation overview; (b) Power Cell Module

exhibits a voltage amplitude of about 46 *Vrms* and a frequency of 50 *Hz* in agreement with the available PV voltage levels. It was desirable to reduce both the currents and voltages by the same factor so that the Joule losses scale with the same factor of the output power. However, the downsizing system was realized considering voltage and current limitations of the different lab sources.

The tests were conducted by using a real-time hardware platform (dSPACE ds1006) consisting of a field programmable gate array (FPGA) and a Processor Board which communicates thought a PHS (Peripheral High Speed) bidirectional bus interface. Each I/O module provides 16 digital channels, 6 A/D channels, and 12 D/A channels. The main FPGA clock has the following characteristics $f_{clk} = 1/T_{clk} = 100MHz$. The FPGAs was programmed using High-Level Synthesis Tool (HLS) blocks. The design of the control and measurement sections was obtained by using, in the MATLAB/Simulink environment, XSG (Xilinx System Generator) tool and dSPACE RTI (Real-Time Interface). The measurement and PWM processes, that need to be executed at higher frequency, were implemented on the FPGA by means of IP blocks from the Xilinx library. Meanwhile, the upper level control, with the PIR controller and the voltage reference signal generation, was implemented on the processor board which is capable of managing its routine and give a new output at $f_{clk,p} = 10kHz$. The FPGA reads the all the measured variables in the A/D channels. Additionally, on the FPGA the carrier waves for the PS-PWM were implemented. In this paper it was chosen $f_{carrier} = 10kHz$. Four different carriers were defined, one for every H-bridge. Each one was 45° out of phase with respect to the previous one. The control pulses were generated on the FPGA. The modulation waveforms were generated in the processor board, they were then re-scaled to be suitable to be compared with such carriers. The current closed-loop control was implemented and the grid connection with PLL was also added. The proposed control system allows supplying active power since the generated current reference is always in phase with the grid voltage. Fig. 10 shows the structure of the control implemented on the d-Space. The black lines indicate the processes that are implemented on the processor board, while the blue lines indicate the processes that are implemented on the FPGA. In the hardware, V_{DC1} and V_{DC2} are connected to the PV simulators while V_{DC3} and V_{DC4} are connected to the power supplies for simulate BESS behavior. The gains, K_i, fixes arbitrary the distribution of maximum desired the AC cell voltage with same grid current between the different H-bridge modules. This allows to control the indirectly the cells power distribution in H-bridge architecture.

B *Experimental results*

Three different tests were performed implementing grid current feedback control with unit power factor: Balanced distribution (Test I), Unbalanced distribution split in Grid power provided by PV and BESS (Test II) and Surplus Power stored in BESS (Test III). The MPPT control of PV sources is not yet implemented since the mail goal is to assess the behavior of PV source and BESS in open loop control for different distribution condition. Table 4 collects the control gains applied in all the evaluations.

B.1. Test I

The first test was performed considering balanced operations between the cells. Table 5 shows the distribution gains (k_i), powers, current, voltages, modulation index and efficiency between the different H-bridge modules. Every source provides about the same amount of power with different efficiency. The total power delivered to the grid is 154 *W* with and overall efficiency of 0.81. Each cell efficiencies were estimated by: $\eta_i = \frac{P_g}{P_{DCi}} k_i$. The modulation index of each cell was evaluated by $m_i = \frac{V_g\sqrt{2}}{V_{DCi}} \frac{k_i}{\cos\varphi}$ where the power factor of output source inverter was 0.92. Fig. 11a shows the grid voltage and the converter voltage on the left axis and the current measurements and reference on the right axis. The converter voltage is obtained from the DC voltage measurements and the switching signals because a very wide bandwidth has been needed to fully acquire the modulated waveform, the voltage drop of IGBT devices was also considered ($V_C E = 1.55V$). The current THD value is around the 13%. In Fig. 11b, the real-time characteristic of P-V, I-V graph of PV sources and mean values of PV powers/currents/voltage are showed. In Fig. 11c the dc-voltage versus time are depicted. As shown, the frequency oscillation of 100 Hz of dc-voltage appears due to the 2nd harmonic of ac instantaneous power. It is reflected into the dc-current, too. In Fig. 11d the mean value of DC-voltage and current of two emulators of BESS are showed.

B.2. Test II

The second test was performed considering unequal distribution between the PV and BESS modules but at the same time equal condition among the two modules of the same kind. Table 6 shows the distribution gains (k_i), powers, current, voltages, modulation index and efficiency between the different H-bridge modules. Every source provides about different amount of power with different efficiency considering their distribution gains. The AC cell voltages of PV sources were obtained with the modulation index of 0.57, while 0.37 for the BESS cells. The power factor of output source inverter was 0.98. The total power delivered to the grid is 154 *W* with and overall efficiency of 0.82. Fig. 12 shows the grid voltage and the converter voltage on the left axis and the

Table 4
EXPERIMENTAL TEST PARAMETERS

Description	Symbol	Value	Unit
Proportional Gain	K_p	5	-
Integral Gain	K_i	10	-
Resonant Gain	K_r	15	-
Inductance	L	5	mH

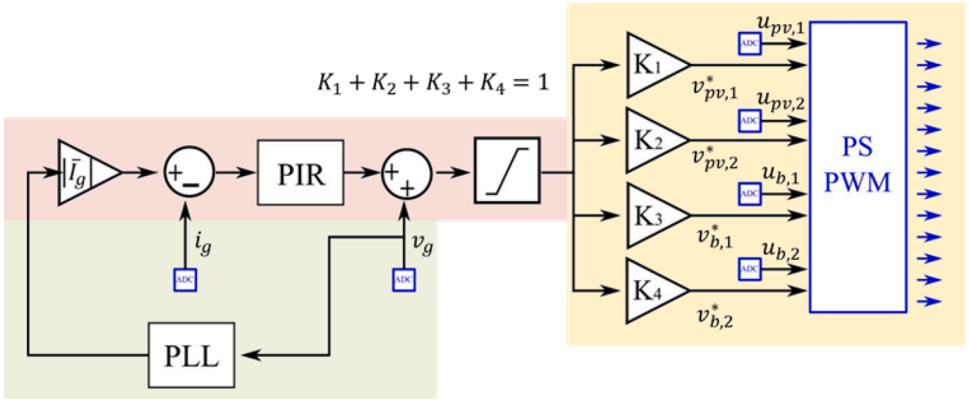

Fig. 10. – Actual implemented control block scheme.

Table 5
MAIN QUANTITIES OF TEST I

MODULE	K_i [p. u.]	V [V]	I [A]	m_i [p. u]	P [W]	Q [VAr]	η_i
PV_1 (DC_1)	0.25	35.4	1.15	0.50	40.7	15.95	0.94
PV_2 (DC_2)	0.25	35.2	1.46	0.50	51.4	20.14	0.74
$BESS_3$ (DC_3)	0.25	36.0	1.29	0.49	46.4	18.20	0.83
$BESS_4$ (DC_4)	0.25	36.0	1.45	0.49	52.4	20.45	0.73
GRID (AC)	-	46.4	3.32	-	154.04	60.37	0.80

current measurements and reference on the right axis. The converter voltage is obtained from the DC voltage measurements and the switching signals because a very wide bandwidth has been needed to fully acquire the modulated waveform, the voltage drop of IGBT devices was a lso considered. The current THD value is around the 14%. In Fig. 12b, the real-time characteristic of P-V, I-V graph of PV sources and mean values of PV powers/current and voltage are showed. In Fig. 11c the dc-voltage versus time are depicted. As shown, the frequency oscillation of 100 Hz of dc-voltage appears due to the 2nd harmonic of ac instantaneous power. It is reflected into the dc-current, too. In Fig. 12d the mean value of DC-voltage and current of two emulators of BESS are showed.

B.3. Test III

The third test was performed with the aim of considering a battery charging condition. Only the $BESS_4$ (active power plow is negative when battery is charged, positive when it is discharged) is charged as shown in Table 7 because the modulating waveforms are always in phase, thus charging two BESS would lead the PV-fed modules to work in over-modulation. Table 6 shows the distribution gains (k_i), powers, current, voltages, modulation index and efficiency between the different H-bridge modules. Every cell provides about different amount of power with different efficiency considering their distribution gains and dc current. The AC cell voltages of PV sources were obtained with the modulation index of 0.87 and 0.88 respectively together with the first BESS cell (0.84), while the last one modulation index of BESS was 0.67 since it was charged. The power factor of output source inverter is 0.97. The total power delivered to the grid is 154 *W* with and overall efficiency of 0.70. In this operating condition the overall efficiency was lower respect the others one since the BESS cells operate at lower efficiencies 0.67 and 0.63 respectively. Thus, the third cell, $BESS_3$, supplies, at the same time, the grid and the cell to be charged. The Fig. 13 shows the grid voltage and the converter voltage on the left axis and the current measurements and reference on the right axis. The current THD value is around 13%. In this test, the modulated waveform does not show the staircase shape which is characteristic of the multilevel inverters. Some of the levels do not appear to be clearly discernible, this is due to the presence of one of the output voltages that is in phase opposition with

Table 6
MAIN QUANTITIES OF TEST II

MODULE	K_i [p. u.]	V [Volt]	I [A]	m_i [p. u.]	P [W]	Q [VAr]	η_i
PV_1 (DC_1)	0.30	35.17	1.46	0.57	51.3	10.21	0.90
PV_2 (DC_2)	0.30	35.0	1.75	0.57	61.1	12.18	0.75
$BESS_3$ (DC_3)	0.20	36.0	1.04	0.37	37.4	7.45	0.82
$BESS_4$ (DC_4)	0.20	36.1	1.05	0.37	37.9	7.54	0.81
GRID (AC)	-	46.4	3.32	-	154.2	30.65	0.82

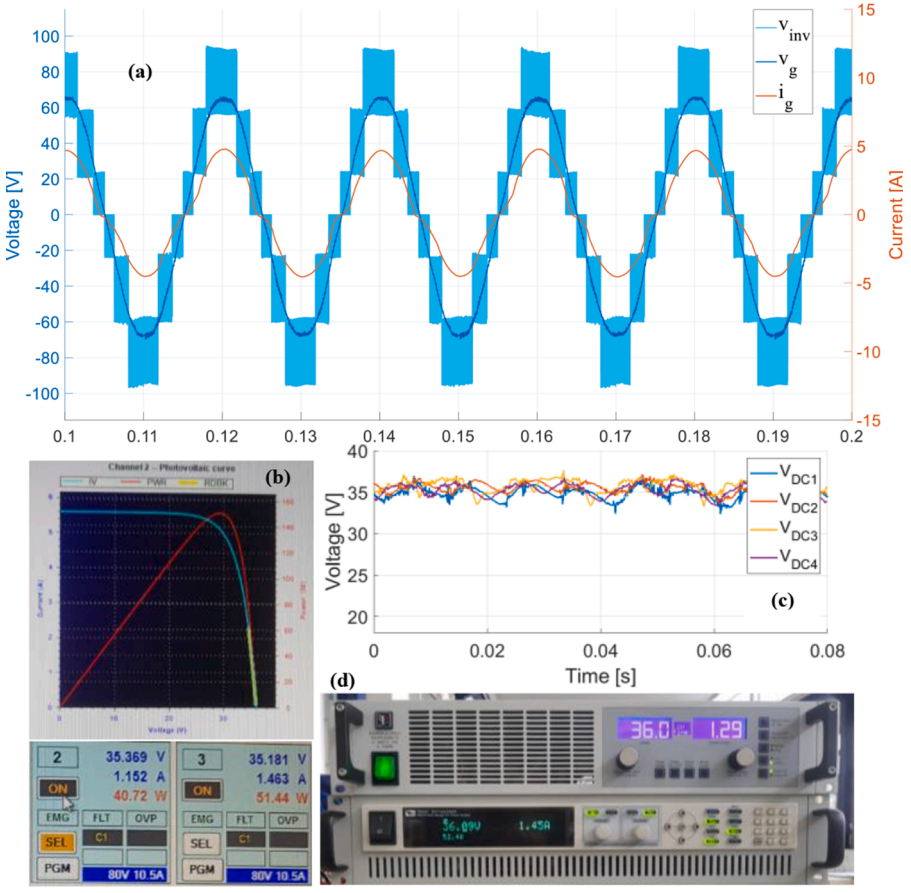

Fig. 11. – Experimental results of Test I: (a) AC grid Voltage and Current vs time, (b) PV Voltage and Current, (c) DC Voltage distribution vs time, (d) BESS Voltage and Current

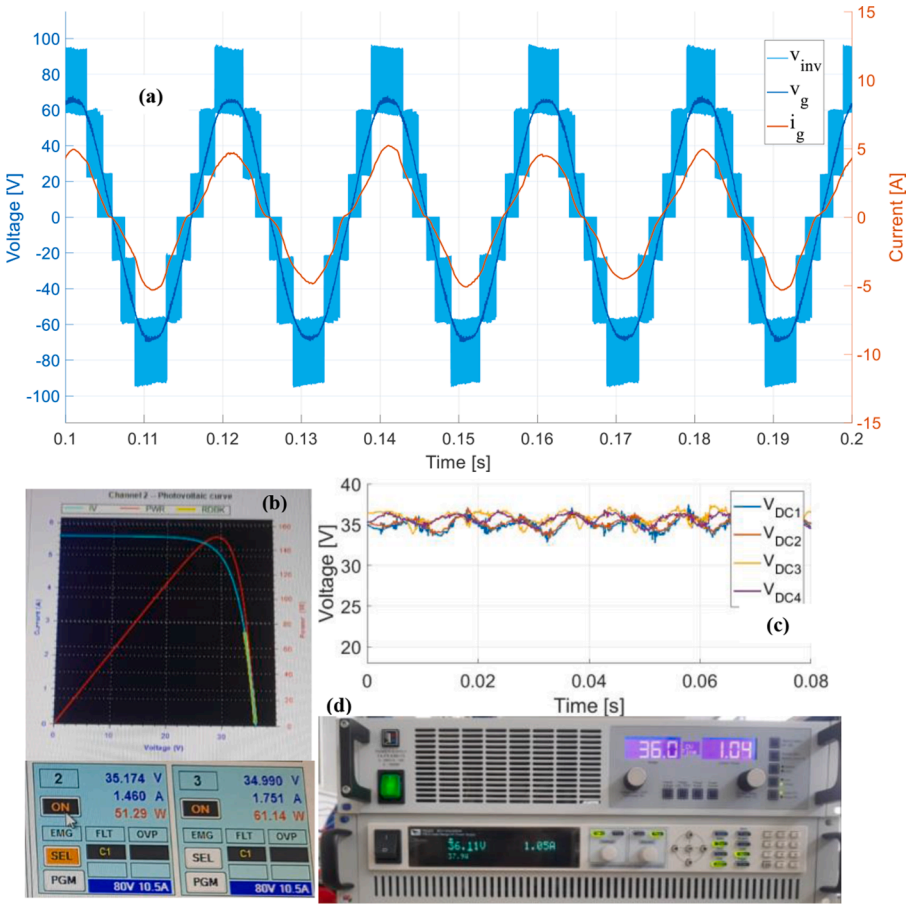

Fig. 12. – Experimental results of Test II: (a) AC grid Voltage and Current vs time, (b) PV Voltage and Current, (c) DC Voltage distribution vs time, (d) BESS Voltage and Current

Table 7
MAIN QUANTITIES OF TEST III

MODULE	K_i [p. u.]	V [Volt]	I [A]	m_i [p. u.]	P [W]	Q [VAr]	η_i
PV_1 (DC_1)	0.45	34.74	2.05	0.87	71.14	17.31	0.97
PV_2 (DC_2)	0.45	34.54	2.31	0.88	79.57	19.39	0.87
$BESS_3$ (DC_3)	0.45	35.9	2.88	0.84	103	25.13	0.67
$BESS_4$ (DC_4)	-0.35	36.0	-0.95	0.65	-34.2	-8.31	0.63
GRID (AC)	-	46.4	3.32	-	154.04	37.45	0.70

the others. The DC voltages related to the PV sources are quite unstable if compared with the previous cases, a clear oscillation is present at the frequency of 100 Hz. This is because the load on those two cells is heavier, but they are not yet working at the MPP, thus the system is working on the steepest section of the V-I characteristic.

In conclusion, for each test carried out it is possible to note the following:

- the number of levels of modulated voltage's inverter are lower than the maximum one ($2N + 1 = 9$). This depend on the operating condition of each module in terms of output voltage. In particular, it depends on the reference voltage (modulating voltage) used by the PS-PMW modulation technique technique. The equivalent reference voltage (PIR output of control block, see Fig. 10) is sinusoidal waveform of 50 Hz, dived by the factor k_i ($i = \cdot\cdot 4$) and then each value is compared with carrier voltage of switching frequency of 10 kHz. In the Figs. 11-13 the number of level are 7 since the maximum amplitude of the equivalent refence voltage is around 81 V (see Figs. 11a,12a, 13a).
- The amplitude difference of level steps of modulated voltage and the number of level used for each modulated valued of modulated voltage depicted in Fig. 13a, respect to previous cases showed in Figs. 11a and 12a, depend by the amplitude oscillation of dc-voltage and the phase opposition of equivalent reference voltage of module $BESS_4$ due to negative sign of the factor coefficient k_4 (see Fig. 10 and Tab.VII). Indeed, it is possible to note that i.e. a value of voltage to be modulated around zero thee level are used ($+22$V, 0V and -22V) instead of two (22V and 0V) This happens also for higher voltage value to be modulated.
- As shown in Tables 5, 6 and 7 the efficiency of each module can change also in significative way for the same overall grid output power. The main reason is due to different the DC powers provided and/or absorbed by each one are keeping the same AC module reference voltages just weighted by factor coefficient k_i and the same AC current imposed by the series of CHB. The consequence is different dc current provided and absorbed by each module with different efficiency.
- In the Figs. 11(b), 12(b and 13(b), the grid current harmonic distortion is observed. In particular, the main harmonic contribution is given by 3rd harmonic current (150 Hz). This is due to the saturation phenomena of feeding transformer. The down-scaled CHB prototype is supplied in low voltage by auto-transformer with a rated power higher then the CHB. This means that the secondary of autotransformer works at very low current close to no-load operation. This accentuates the phenomenon of saturation in the iron of the autotransformer, so the third harmonic component appears in the

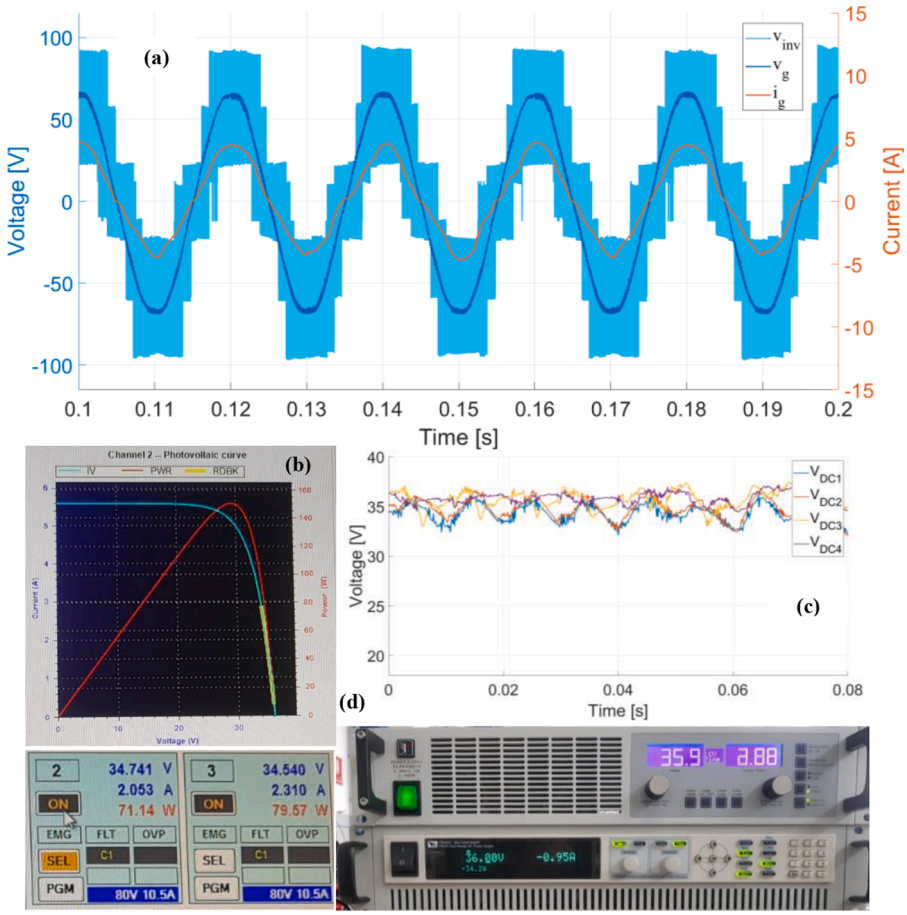

Fig. 13. – Experimental results of Test III: (a) AC grid Voltage and Current vs time, (b) PV Voltage and Current, (c) DC Voltage distribution vs time,(d) BESS Voltage and Current

magnetic induction filed and therefore in the voltage. Being the single-phase system, it also affects the current. Then we also observe phenomena on the current i.e. variation of the maximum amplitude, linked to oscillations of the regulator output in its proportional part.

8. Conclusions

This paper has been focused on the energy management strategy of PV-BESS hybrid systems using a single CHB inverter topology for residential applications. In ideal conditions, the system should work with the CHB in unitary power factor and with all the PV modules at their MPP. However, this is not always possible because of some functional constraints acting on the system. For this reason, the energy management strategy is based on the solving an optimal problem in terms of minimization of the grid reactive power, of the photovoltaic and the battery modules and to maximize the PV production. The battery integration plays a role of compensating power fluctuation due to the stochastic nature of PV production. This latter allows us to smooth a short-term PV variability by providing both a dynamic energy buffer and coordination of power supply and demand. In the proposed approach, a centralized and distributed control system architecture, using different priority layers (upper and lower) has been adopted. The steady-state voltage and current references have been computed by solving a multi-objective optimization problem, which has been explicitly formalized considering both the technical constraints of the system and different functional requirements, the latter having different priority levels according to the operating conditions of the converter. An equivalent circuit modelling approach has been used for the control implementation. A campaign of simulated performance has been conducted to show the operating limits of the PV-BESS CHB architecture using different weights in order to highlights how these limits can be overcome. Good system performance proves the effectiveness of the proposed design and control method. Finally, experimental set-up has been presented on laboratory prototype in order to assess the operating conditions feasibility of proposed CHB architecture and its overall efficiency considering cell electrical constraints.

Declaration of Competing Interest

The authors declare that they have no known competing financial interests or personal relationships that could have appeared to influence the work reported in this paper.

Data availability

No data was used for the research described in the article.

References

[1] M. Salehi, M. Shahabadini, H. Iman-Eini, M. Liserre, Predictive control of grid-connected modified-CHB with reserve batteries in photovoltaic application under asymmetric operating condition, IEEE Transactions on Industrial Electronics 69 (9) (Sept. 2022) 9019–9028.
[2] P.T. Krein, J.A. Galtieri, Active management of photovoltaic system variability with power electronics, IEEE Journal of Emerging and Selected Topics in Power Electronics 9 (6) (Dec. 2021) 6507–6523.
[3] W. Liang, Y. Liu, J. Peng, A day and night operational quasi-z source multilevel grid-tied PV power system to achieve active and reactive power control, IEEE Transactions on Power Electronics 36 (1) (Jan. 2021) 474–492.

[4] C.-Y. Tang, P.-T. Chen, J.-H. Jheng, Bidirectional power flow control and hybrid charging strategies for three-phase PV power and energy storage systems, IEEE Transactions on Power Electronics 36 (11) (Nov. 2021) 12710–12720.
[5] S. Kumar, L.N. Patel, B. Singh, A.L. Vyas, Self-adjustable step-based control algorithm for grid-interactive multifunctional single-phase PV-battery system under abnormal grid conditions, IEEE Transactions on Industry Applications 56 (3) (May-June 2020) 2978–2987.
[6] Y. Pan, A. Sangwongwanich, Y. Yang, X. Liu, M. Liserre, F. Blaabjerg, Flexible active power control of distributed photovoltaic systems with integrated battery using series converter configurations, IEEE Journal of Emerging and Selected Topics in Power Electronics (Dec 2021).
[7] S.M. Goetz, C. Wang, Z. Li, D.L.K. Murphy, A.V. Peterchev, Concept of a distributed photovoltaic multilevel inverter with cascaded double H-bridge topology, Int. J. Electr. Power Energy Syst. 110 (2019) 667–678.
[8] U. Sohail, H. Nademi, L.E. Norum, A Reliable Modular Based PV-Battery Hybrid System with Peak Shaving Capability, in: 2018 IEEE 19th Workshop on Control and Modeling for Power Electronics (COMPEL), Padua, Italy, 2018, pp. 1–6.
[9] T. Strasser, et al., A review of architectures and concepts for intelligence in future electric energy systems, IEEE Transactions on Industrial Electronics 62 (4) (April 2015) 2424–2438, https://doi.org/10.1109/TIE.2014.2361486.
[10] S. Lakshminarayana, T.Q.S. Quek, H.V. Poor, Cooperation and storage tradeoffs in power grids with renewable energy resources, IEEE Journal on Selected Areas in Communications 32 (7) (July 2014) 1386–1397, https://doi.org/10.1109/JSAC.2014.2332093.
[11] X. Li, L. Yao, D. Hui, Optimal control and management of a large-scale battery energy storage system to mitigate fluctuation and intermittence of renewable generations, Journal of Modern Power Systems and Clean Energy 4 (4) (October 2016) 593–603, https://doi.org/10.1007/s40565-016-0247-y.
[12] B. Xiao, L. Hang, J. Mei, C. Riley, L.M. Tolbert, B. Ozpineci, Modular cascaded H-bridge multilevel PV inverter with distributed MPPT for grid-connected applications, IEEE Trans. Ind. Appl. 51 (2) (2015) 1722–1732. Mar./Apr.
[13] M. Coppola, P. Guerriero, D. Iannuzzi, S. Daliento, A. Del Pizzo, Extended operating range of PV module-level CHB inverter, International Journal of Electrical Power & Energy Systems 119 (2020), 105892.
[14] H. Mahmood, D. Michaelson, J. Jiang, Decentralized power management of a PV/battery hybrid unit in a droop-controlled islanded microgrid, IEEE Trans. Power Electron. 30 (12) (Dec. 2015) 7215–7229.
[15] F. Rong, X. Gong, S. Huang, A novel grid-connected PV system based on MMC to get the maximum power under partial shading conditions, IEEE Trans. Power Electron. 32 (6) (2017) 4320–4333.
[16] E. Villanueva, P. Correa, J. Rodriguez, M. Pacas, Control of a single-phase cascaded H-bridge multilevel inverter for grid- connected photovoltaic systems, IEEE Trans. Ind. Electron. 56 (11) (2009) 4399–4406.
[17] Y. Fayyad, L. Ben-Brahim, Multilevel cascaded Z source inverter for PV power generation system, in: Int. Conf. on Renewable Energy Research and Applications, Nagasaki, 2012, pp. 1–6.
[18] Z. Wang, S. Fan, Y. Zheng, M. Cheng, Design and analysis of a CHB converter based PV-battery hybrid system for better electromagnetic compatibility, IEEE Transactions on Magnetics 48 (11) (Nov. 2012) 4530–4533, https://doi.org/10.1109/TMAG.2012.2198912.
[19] I. Abdalla, J. Corda, L. Zhang, Multilevel DC-link inverter and control algorithm to overcome the PV partial shading, IEEE Trans. Power Electron. 28 (1) (2013) 14–18.
[20] Erol Can, A new multi-level inverter with reverse connected dual dc to dc converter at simulation, International Journal of Modelling and Simulation 42 (1) (2022) 34–46, https://doi.org/10.1080/02286203.2020.1824451.
[21] R. Uthirasamy, V. Kumar Chinnaiyan, U.S. Ragupathy, J. Karpagam, Investigation on three-phase seven-level cascaded DC-link converter using carrier level shifted modulation schemes for solar PV system applications, IET Renew. Power Gener. 12 (4) (2018) 439–449.
[22] R. Cuzmar, J. Pereda, R. P. Aguilera, Phase-shifted model predictive control to achieve power balance of CHB converters for large-scale photovoltaic integration," in, IEEE Transactions on Industrial Electronics, doi:10.1109/TIE.2020.3026299.
[23] B. Xu, H. Tu, Y. Du, H. Yu, H. Liang, S. Lukic, A distributed control architecture for cascaded H-bridge converter with integrated battery energy storage, IEEE Transactions on Industry Applications 57 (1) (Jan.-Feb. 2021) 845–856, https://doi.org/10.1109/TIA.2020.3039430.
[24] C. Sirico, R. Teodorescu, D. Séra, M. Coppola, P. Guerriero, D. Iannuzzi, A. Dannier, PV module-level CHB inverter with integrated battery energy storage system, Energies 12 (2019), 4601, https://doi.org/10.3390/en12234601.
[25] Q. Zhang, K. Sun, A flexible power control for PV-battery hybrid system using cascaded H-bridge converters, IEEE Journal of Emerging and Selected Topics in Power Electronics 7 (4) (Dec. 2019) 2184–2195, https://doi.org/10.1109/JESTPE.2018.2887002.
[26] P. Liu, S. Duan, Derivation of the generalized phase-shifted angles by using phasor diagrams for the CHB converter with unbalanced DC voltage sources," in, IEEE Transactions on Industrial Electronics, doi:10.1109/TIE.2020.3040674.
[27] E. Can, H.H. Sayan, A novel SSPWM controlling inverter running nonlinear device, Electrical Engineering 100 (1) (2018) 39–46.
[28] Erol Can, Hasan Hüseyin Sayan, Development of fractional sinus pulse width modulation with β gap on three step signal processing, International Journal of Electronics (2022), https://doi.org/10.1080/00207217.2022.2040056.
[29] E. Can, The levels effect of the voltage generated by an inverter with partial source on distortion, International Journal of Electronics 107 (9) (2020) 1414–1435.
[30] J.M. Guerrero, P.C. Loh, T.L. Lee, M. Chandorkar, Advanced control architectures for intelligent microgrids-part II: power quality energy storage and AC/DC microgrids, IEEE Trans. Ind. Electron. 60 (4) (2013) 1263–1270.